applied sciences

MDPI

Article

Prism-Based Spatial Heterodyne Spectrometer with a Fixed Fringe Localization Plane

Zihao Liu [1,2], Da Zhang [1,3,*], Huanyu Yang [1,2] and Chunling Huo [1,2]

[1] Changchun Institute of Optics, Fine Mechanics and Physics, Chinese Academy of Sciences, Changchun 130033, China; liuzihao221@mails.ucas.ac.cn (Z.L.); yanghuanyu16@mails.ucas.ac.cn (H.Y.); huochunling16@mails.ucas.ac.cn (C.H.)
[2] University of Chinese Academy of Sciences, Beijing 100049, China
[3] Materials and Optoelectronics Research Center, University of Chinese Academy of Sciences, Beijing 100049, China
* Correspondence: zhangda@ciomp.ac.cn; Tel.: +86-139-4410-2067

Abstract: Spatial heterodyne spectroscopy (SHS) based on prism dispersion is a novel technique designed to overcome the limitations of traditional grating-based SHS, which is affected by grating diffraction. However, there are still some challenges with this technique, one of which is that the fringe localization plane (FLP) moves with changes in wavelength. This paper proposes a prism-based tunable SHS where the FLP is fixed, utilizing prism–bimirror–mirror structures. The theoretical spectral resolving power, based on an example, is higher than 1300 in the spectral range from 10,000 cm^{-1} to 25,641 cm^{-1} and is approximately 27,595 at 25,641 cm^{-1}. Furthermore, we propose solutions to simplify the motion control system and address the problem of spectral aliasing.

Keywords: spatial heterodyne spectrometer; interferometers; Fourier transforms; spectroscopy

1. Introduction

In 1971, spatial heterodyne spectroscopy (SHS) was pioneered at Osaka University in Japan [1]. SHS offers superior robustness and higher spectral resolving power compared to traditional Fourier-transform spectroscopy, making it a focal point in spectroscopy research [2]. Typically, SHS employs gratings as dispersion elements [3–15], but these gratings can introduce several challenges. Firstly, multiple diffraction orders disperse energy across different orders. To prevent inter-order disturbances, a baffling system needs to be set and in some cases this baffling system can be only partially effective [16]. Secondly, Matthias Lenzner et al. point out that an interferogram is formed by wave packets with a titled energy front when diffracted from gratings, and this fact limits spectral resolving power [17]. Thirdly, in tunable spatial heterodyne spectrometers (TSHSs) using blazed gratings, adjusting the Littrow angle by tilting the gratings widens the spectral range but reduces energy in interfering beams by deviating from the gratings' blaze angle. Fourthly, compared to prisms, gratings generally generate more diffuse light [18].

Due to the above limitations of grating-based SHSs, prism-based SHSs have increasingly captured researchers' interest in recent years. In 2019, Ye Song et al. proposed a prism-based SHS, replacing the grating used in traditional SHSs with a prism–mirror structure [19]. In 2021, Fabio Frassetto et al. experimentally demonstrated the beneficial effects on the signal-to-noise ratio that the substitution of gratings with prisms produces in a SHS [16]. In 2022, Li Yixuan et al. proposed an orthogonal TSHS, utilizing a Prism–Mirror instead of a grating and designing an orthogonal configuration to simplify the motion control system [20]. In 2024, Fabio Frassetto et al. designed a prism-based monolithic

check for updates

Academic Editors: Andrés Márquez and Matt Oehlschlaeger

Received: 5 December 2024
Revised: 25 December 2024
Accepted: 8 January 2025
Published: 9 January 2025

Citation: Liu, Z.; Zhang, D.; Yang, H.; Huo, C. Prism-Based Spatial Heterodyne Spectrometer with a Fixed Fringe Localization Plane. *Appl. Sci.* **2025**, *15*, 598. https://doi.org/10.3390/app15020598

SHS by coating prisms with mirrors [18]. These prism-based SHS designs all leverage prism–mirror structures.

Although prism-based SHS has a higher signal-to-noise ratio under certain conditions, this technology is currently immature. The fact that prism dispersion is based on Snell's law and the nonlinear relationship between wavelength and refractive index limits the instrument's usable Field-of-View (FOV), especially in the direction of dispersion, and spectral resolving power, especially at long wavelengths. There is still a lack of research on the FOV and methods to improve the spectral resolving power of prism-based SHS. In addition, the location of the fringe localization plane (FLP) varies with incident light wavelength. The FLP is where the interference fringes can be viewed with maximum clarity, so the fringes can be obtained at maximum contrast at this plane [5]. To observe fringes, the FLP must be optically conjugated to the detector plane using an imaging system. Therefore, if the incident light lacks spatially full coherence, the fringe contrast on the detector degrades when the FLP is not precisely conjugated with the detector plane. Fabio Frassetto et al. [18] also noted that the instrumental response changes as the FLP location varies with wavelength. This paper focuses on the problem of the movement of the FLP and proposes a design to address it.

2. Principles and Designs

2.1. Movement of the FLP in Prism-Based SHSs

The principle of prism-based SHSs and the phenomenon of the movement of the FLP are briefly described using a typical prism-based SHS [19]. As shown in Figure 1, it is based on a Michelson interferometer modified by replacing the mirror in each arm with a prism–mirror assembly. Both mirrors are tilted at the same angle with respect to the prisms in their respective arms. The collimated light enters the beam splitter and is divided into two beams. The beam in each arm passes sequentially through the prism, mirror, prism again, and then returns to the beam splitter. The beam with a certain wavelength, called the Littrow wavelength, will incident perpendicular to the mirror and return parallel to the optical axis. The wave fronts with the Littrow wavelength exiting from the interferometer are perpendicular to the optical axis and produce an interferogram with zero frequency. For a wavelength different from the Littrow wavelength, since the prism has different refractive indices at different wavelengths, the wave fronts of the two outgoing beams are no longer parallel, but tilt at the same angle relative to the optical axis in opposite directions, equivalently producing fringes on the FLP. The FLP can be visualized as a plane of recombination of the two backpropagating beams exiting from the interferometer and should be imaged by the imaging system onto the detector plane.

For traditional grating-based SHSs, the location of the FLP is very intuitive as the beam in each arm is diffracted by the grating only once, so the FLP intersects the center of each grating. However, for the SHSs with a prism–mirror structure, the beam in each arm is refracted more than once by the prism, so there is uncertainty in the location of the recombination plane obtained by extending the outgoing rays from the two arms in the reverse direction. For example, if the apex angle of the prism is set to 30°, the height of the prism is set to 25 mm, the material is set to N-LASF9, the length of the optical axis between the prism and the mirror is set to 16.2 mm, and the Littrow wavelength is 650 nm, the distances from the FLP to the entering surface of the prism if the wavelengths of the incident ray are 400 nm, 600 nm, and 1000 nm are, respectively, about 73.6 mm, 83.5 mm, and 88.6 mm. It can be seen that the location of the FLP is different for different wavelengths of the incident ray, which is consistent with the phenomenon in the experiments done by Fabio Frassetto et al. [18]: when focusing the imaging optics on a particular FLP distance, a spectral response peaking was obtained at that corresponding wavelength. In fact, the

FLP of a point source (ideally) is unlocalized, except that the size of the overlap region of the beams from the two arms varies at different locations. However, even a laser is not an ideal point source and the FLP is localized [5]. Maintaining a fixed FLP can eliminate the need to calculate the FLP's location and move the imaging device based on the predicted wavelength of the incident light during use.

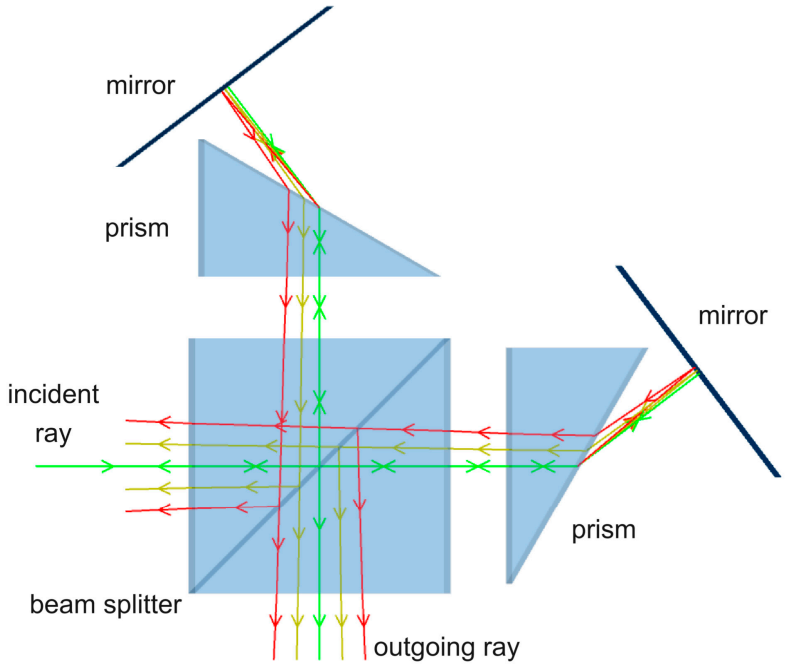

Figure 1. Layout of the interferometer of a typical prism-based spatial heterodyne spectrometer (SHS) [19]. A point source containing three wavelengths is set. Arrows of different colors represent rays with different wavelengths.

2.2. Preliminary Optical Design

To keep the location of the FLP constant, we can make the optical axes of the two arms be turned in opposite directions with respect to each other only once due to refraction. This requires the beam in each arm to pass through the prism only once. After the beam passes through the prism, it needs to return to the beam splitter without passing through the prism again. Therefore, some form of optics is needed to reflect the beam and provide a shift.

To realize this idea, we propose to use a prism–bimirror–mirror assembly instead of the prism–mirror structure in each arm, as shown in Figure 2a, with the angle made by the two planes of the bimirror being a right angle. The collimated light is split by a beam splitter and is divided into two paths. Now we will describe only one of the paths. The beam is incident vertically into a prism and refracted at its exiting surface. Then, the beam is incident to one of the planes of the bimirror. The intersection line of the two planes of the bimirror is perpendicular to the incoming axis of the bimirror and parallel to the side surfaces of the prism. In terms of the direction of the beam, a right-angle bimirror is equivalent to a mirror, except that the beam is shifted by an extra segment of the optical axis between the incoming and outgoing axes, which staggers the incoming and outgoing beams.

To allow the beam to return to the beam splitter for recombination with another one, a mirror is added behind the bimirror to change the direction of the optical axis. This mirror is tilted at a proper angle so that its outgoing optical axis is perpendicular to the surface of the cube beam splitter. The system is a TSHS in which the Littrow wavelength can be tuned by tilting the bimirrors and the mirrors. The rotating spindle is located at the refracting

surface of the prism, intersecting the center of the refracting surface, as well as at the mirror, intersecting the center of the mirror. The bimirror and mirror share this spindle, where the bimirror needs to be tilted twice as much as the mirror during the tuning process. The prism–bimirror–mirror structures of the two arms are upside down with respect to each other in order to ensure that the outgoing beams from the two arms are tilted in opposite directions, as shown in Figure 2b.

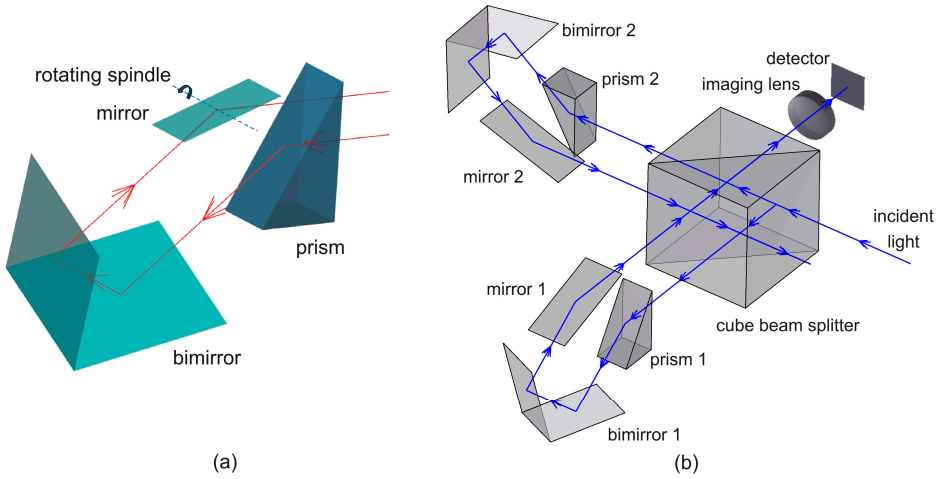

Figure 2. (**a**) Schematic diagram of the prism–bimirror–mirror structure. The angle between the two mirrors of the bimirror is 90°. (**b**) Layout of the tunable spatial heterodyne spectrometer (TSHS) using a prism–bimirror–mirror structure.

If the wavelength of the incident light is not equal to the tuned Littrow wavelength, the wave fronts of the beams of the two arms are tilted by the same angle relative to the optical axis in opposite directions, equivalently producing the fringes on the FLP. The center of the FLP overlaps with the center of the refracting surface of each prism. The distance from the FLP to the imaging optics is equal to the length of the optical axis between the refracting surface of each prism and the imaging optics. This length does not change, regardless of the tuned Littrow wavelength and the wavelength of the incident light, solving the problem of the FLP location varying with the wavelength that exists in current prism-based SHS designs.

Besides diffused light, stray light can be generated by specular reflection on the surfaces of the cube beam splitter and prisms. Anti-reflection (AR) coatings are needed to improve transmittance. In the arrangement shown in Figure 2, the splitting and recombination of the beams occur at different locations in the beam splitter, preventing the beams from reaching the detector without passing through any arm. In addition, the prisms are single- rather than double-passed, which may result in less chance for the beams to be reflected by the prisms. Stray light analysis requires the consideration of many other factors such as mechanical structure and still requires further research.

An added advantage of this system is that the outgoing beams in the two different directions are not backtracking toward the source. The two outgoing beams can be detected by two detectors to increase the luminous flux. This advantage remains if the prisms are replaced by gratings, which is not discussed further in this paper.

2.3. Spectral Inversion

The parameters of the key components in the Zemax OpticStudio v.19.4 simulation are provided here first. The glass of each prism used is N-LASF9 (SCHOTT Group Corporation, Mainz, Germany) and the apex angle of each prism is 30°. The half-width of the incident light is 20 mm. The imaging system has a magnification of 0.5. The parameters of the

detector refer to the SONY IMX 174 (Sony Group Corporation, Tokyo, Japan), which has a pixel pitch of 5.86 μm and 1936 × 1216 pixels.

Assuming that the wavelength of the incident light is not equal to the tuned Littrow wavelength, the equivalent fully transmissive optical system is shown in Figure 3a and the wave fronts intersecting the centers of the refracting surfaces of the prisms of the two arms are shown in Figure 3b. Assuming points A and B on the two wave fronts are from any point on the light source, the two beams propagate in the directions AC and CB, respectively. They are equivalent to intersecting at point C. Thus, the FLP intersects the center of the refracting surface of each prism and is perpendicular to the outgoing optical axis of each prism. The center of interference is always located at the center of the FLP and the values of the optical path difference (OPD) at both ends of the FLP are the largest.

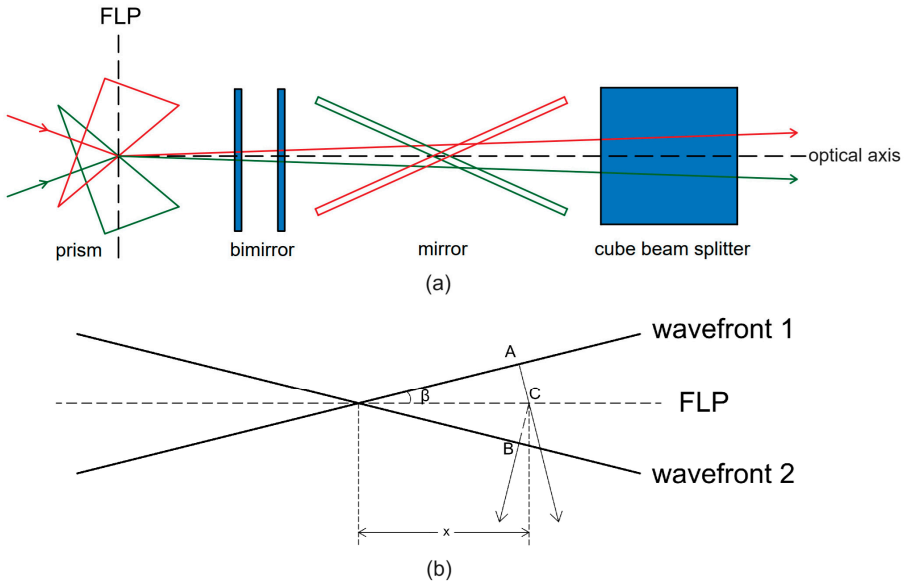

Figure 3. (**a**) Schematic diagram of the equivalent fully transmissive model of the two arms of the interferometer using a prism–bimirror–mirror structure. The red arrows and optics represent the ray in one arm and the optics it passes through, while the green arrows and optics represent the ray in the other arm and the optics it passes through. The blue optics represent the optics that the ray in each of the two arms passes through. (**b**) Schematic diagram of the wave fronts intersecting the centers of the refracting surfaces of the prisms of the two arms.

If the angle between each wave front and the FLP is β, then the *OPD* is

$$OPD = AC + CB = 2x\sin\beta \tag{1}$$

Then, the spatial frequency f of the interferogram is

$$f = 2\sigma\sin\beta \tag{2}$$

where σ is the wavenumber of the incident light, which is the reciprocal of the wavelength λ. Setting the Littrow wavelength as λ_0, the angle β between the wave front and the FLP is

$$\beta = \sin^{-1}(n(\lambda_0)\sin(30^\circ)) - \sin^{-1}(n(\lambda)\sin(30^\circ)) \tag{3}$$

The refractive index n versus wavelength λ equation for the N-LASF9 provided in the Glass Catalog of ZEMAX is

$$n(\lambda)^2 - 1 = \frac{K_1\lambda^2}{\lambda^2 - L_1} + \frac{K_2\lambda^2}{\lambda^2 - L_2} + \frac{K_3\lambda^2}{\lambda^2 - L_3} \tag{4}$$

The coefficients of the formula are K_1 = 2.00029547, L_1 = 0.0121426017 μm^2, K_2 = 0.298926886, L_2 = 0.0538736236 μm^2, K_3 = 1.80691843, and L_3 = 156.530829 μm^2. The correspondence between the spatial frequency f of the interferogram on the FLP and the wavelength λ of the incident light has been established up to this point. Compared to the SHS with a prism–mirror structure, it has a much simpler inversion formula.

2.4. Performance Parameters

Now, we calculate the theoretical spectral resolving power of the system. Assuming that the incident light with a wavenumber of σ_1 produces 2N fringes, the maximum *OPD* on the interferogram can be expressed as $N\lambda_1$. If the half-width of the light source is d_0, due to the small angle between the wave fronts of the two arms and the FLP, the half-width d of the wave fronts of the two arms after passing through the refracting surfaces of the prisms can be approximated as

$$d(\sigma_0) = \frac{d_0}{\cos 30^\circ} \times \sin\left(90^\circ - \sin^{-1}(\sin(30^\circ)n(\sigma_0))\right) \tag{5}$$

Thus, the maximum *OPD* can also be expressed as

$$OPD_{\max} = N\lambda_1 = 2d(\sigma_0)\sin\beta_1 \tag{6}$$

where β_1 is the angle between each wave front and the FLP when the wavelength of the incident light is λ_1. Since β_1 is small, substituting Equation (3) into Equation (6), we can approximately get

$$N = 2d(\sigma_0)\sigma_1\left(\sin^{-1}(0.5n(\sigma_0)) - \sin^{-1}(0.5n(\sigma_1))\right) \tag{7}$$

Assuming that the number of fringes increases by one when the wavenumber of the incident light changes to σ_2, the same way we obtain

$$N + 0.5 = 2d(\sigma_0)\sigma_2\left(\sin^{-1}(0.5n(\sigma_0)) - \sin^{-1}(0.5n(\sigma_2))\right) \tag{8}$$

The difference between these two wavenumbers is the maximum spectral resolution. When defining the function,

$$f(\sigma) = \sigma\sin^{-1}(0.5n(\sigma)) \tag{9}$$

Combining Equation (7) and Equation (8), we can get

$$0.25 = d(\sigma_0)\left((\sigma_2 - \sigma_1)\sin^{-1}(0.5n(\sigma_0)) - (f(\sigma_2) - f(\sigma_1))\right) \tag{10}$$

Since the difference between σ_1, σ_2 and σ_0 is small at a given tuning, the following approximation can be made:

$$f(\sigma_2) - f(\sigma_1) = f'(\sigma_0)(\sigma_2 - \sigma_1) \tag{11}$$

where $f'(\sigma)$ denotes the derivative function of $f(\sigma)$. Substituting Equation (11) into Equation (10), we can get the maximum spectral resolution:

$$\sigma_2 - \sigma_1 = \frac{1}{4d(\sigma_0)\left(\sin^{-1}(0.5n(\sigma_0)) - f'(\sigma_0)\right)} \tag{12}$$

The theoretical spectral resolving power of the system at wavenumber σ can be expressed by the following equation:

$$R = \frac{\sigma}{\delta\sigma} = 4\sigma d(\sigma)\left(\sin^{-1}(0.5n(\sigma)) - f'(\sigma)\right) \tag{13}$$

The variation of the theoretical spectral resolving power of the spectrometer is shown in Figure 4. The theoretical spectral resolving power in the spectral range (10,000 cm^{-1}~25,641 cm^{-1}) is approximately 1381~27,595; that is, the highest spectral resolution is approximately 0.014 nm/390 nm (0.93 cm^{-1}/25,641 cm^{-1}). In some applications, the required spectral resolving power differs in different spectral ranges, allowing the selection of the appropriate material and apex angle for the prisms accordingly.

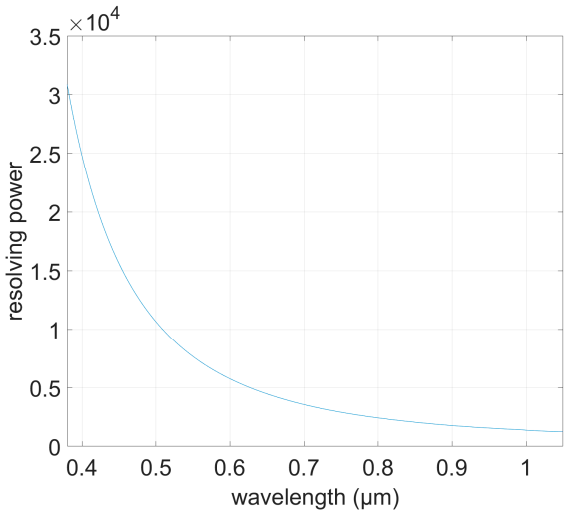

Figure 4. Theoretical spectral resolving power curve of the TSHS with a prism–bimirror–mirror structure for the given parameters.

Next, consider the tuning angles of the system. According to the Nyquist–Shannon theorem, spectral information can be recovered if a detector uniformly samples an interferogram at a frequency that exceeds the fringe frequency by at least a factor of two. The spectral range of an arbitrary tuning is limited by the maximum fringe frequency of the interferogram, which is determined by the pixel pitch of the detector. In the simulation in this paper, six tuning steps are required to achieve detection in the range of 0.39 μm to 1 μm: the angles of the mirror tilt with respect to its outgoing optical axis are 20.99°, 20.51°, 20.01°, 19.44°, 18.78°, and 18.19°, respectively corresponding to Littrow wavelengths of 0.398 μm, 0.420 μm, 0.450 μm, 0.500 μm, 0.600 μm, and 0.800 μm. The bimirror is tilted at twice the angle of the mirror to ensure that its outgoing optical axis is aligned with the incoming optical axis of the mirror.

Finally, consider the usable FOV. In SHS, the limiting off-axis angles are reached when the OPD at the edge of the fringe pattern changes by 1/2 wavelength. Since the usable FOV is negatively correlated with the spectral resolving power, the usable FOV when the incident light is at the wavelength with maximum spectral resolving power (0.39 μm)

determines the usable FOV of the instrument. By setting the conditions to get a series of solutions and fitting the relationship between ϕ and φ,

$$\frac{\phi^2}{(0.06^\circ)^2} + \frac{\varphi^2}{(0.20^\circ)^2} \leq 1 \tag{14}$$

where ϕ denotes the angle between the on-axis rays and the component of the off-axis rays in the dispersion plane and φ denotes the angle between the off-axis rays and the dispersion plane. The FOV of this system is comparable to that of the typical prism-based SHS shown in Figure 1 in cases of equal spectral resolving power.

2.5. Simplification of the Motion Control System

Tuning the spectrometer with the structure shown in Figure 2 requires tilting four optics: two bimirrors and two mirrors. The motion control system is more complex than that of a grating-based TSHS, which requires tilting only two gratings. We drew on the orthogonal interferometer based on a Michelson interferometer designed by Li Yixuan et al. [20] and modified it into the form of a Mach–Zehnder interferometer. After simplifying the motion control system, it allows tuning by tilting only two optics at the expense of a larger spectrometer size. As shown in Figure 5a, the collimated light is divided by the beam splitter into arm A and arm B. Arm A contains mirror 1 and arm B contains a bimirror. The angle between the two mirrors of the bimirror is 90°. The mirror 1 and bimirror, each placed at 22.5°, reflect the beams onto a right-angle prism coated with mirrors. Then the two beams incident parallelly to prism 1 and prism 2, respectively. The bimirror acts like a roof prism, deflecting the beam top-to-bottom.

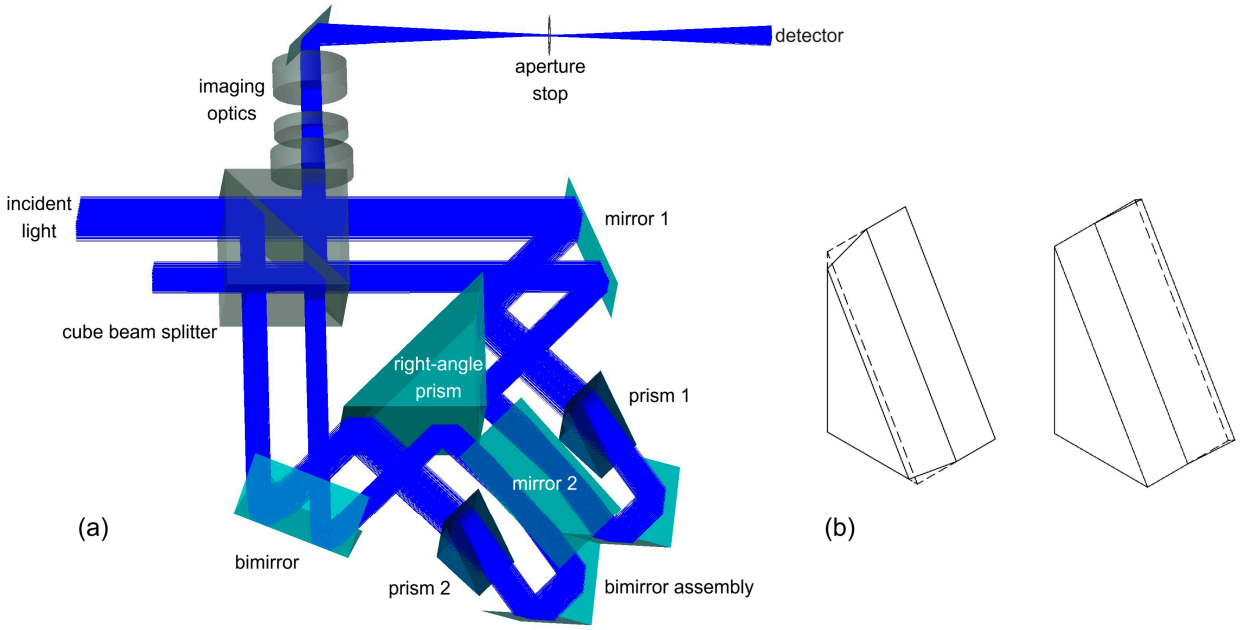

Figure 5. Improvements on the preliminary design. (**a**) Layout of the spectrometer after simplifying the motion control system. (**b**) Schematic diagram of the anti-aliasing prisms of the two arms. The tilting angle of the half-surfaces is exaggerated in this diagram. As a comparison, the dashed lines show the shape before modification.

When the beams of the two arms are incident into the prisms placed in the same direction, the cross-section of the beam of arm B is upside down. Thus, while the two beams are refracted by the prisms in a same outgoing direction, they are equivalent to being tilted at the same angle relative to the optical axis in opposite directions. After this,

the beams of the two arms pass through the bimirror assembly and mirror 2 and return to the right-angle prism in turn. Then, the beam of arm A passes through mirror 1 again and the beam of arm B passes through the bimirror again, being deflected bottom-to-top. Finally, the two beams return to the beam splitter for recombination.

This modified structure assembles the two bimirrors of the two arms of the prism–bimirror–mirror TSHS into a bimirror assembly by fixing them together and tilting them synchronously. Similarly, the two mirrors of the two arms are combined into mirror 2. Therefore, tuning can be performed by simply tilting the bimirror assembly and mirror 2 around the rotating spindle, simplifying the motion control system.

2.6. Anti-Aliasing Design

One of the major limitations of SHS is that the symmetry in achieved spectrum from the Fourier transform duplicates all spectrum features at locations on either side of the Littrow wavelength λ_0, which is referred to as aliasing. If $\lambda_1 > \lambda_0$, the spatial frequency f of the interferogram corresponds to λ_1 one-to-one; if $\lambda_2 < \lambda_0$, f also corresponds to λ_2 one-to-one. Therefore, a spatial frequency f corresponds to two wavelengths, λ_1 and λ_2. We need an additional mechanism to tell the difference between λ_1 and λ_2.

For grating-based SHSs, each grating can be tilted by a small, constant angle around the axis of symmetry which is perpendicular to the tuning spindle. This tilting produces a constant frequency in a direction orthogonal to the interference fringes generated by dispersion. However, in prism-based SHSs, if the mirrors are tilted, the FLP of the fringes produced by dispersion is at a different location than the FLP of the fringes orthogonal to the direction of dispersion. If the prisms are tilted, this will lead to a change in the refractive angle, which may have an effect on the accuracy of the spectrum [20]. This is acceptable if the resolution of the spectrometer is not very high.

We consider tilting only half of the areas of the refracting surfaces of the prisms of both arms by a small angle (0.1°) around their axes of symmetry which are perpendicular to the tuning spindle, as shown in Figure 5b. This results in both a 1D interferogram and a 2D interferogram on the FLP, where the 1D interferogram recovers the exact spectrum and the 2D interferogram is used to differentiate between λ_1 and λ_2. Now, we describe the principle of the 2D interferogram. The beams pass through half of the refracting surfaces that are tilted and not only produce the angle β with the optical axis in the dispersion plane, but also produce an angle γ with the optical axis in the direction orthogonal to the dispersion plane. When the beams are recombined by the beam splitter, the angles become $+\gamma$ and $-\gamma$, because the beam from one arm is transmitted and the beam from the other arm is reflected. The plus or minus sign of γ is determined by which arm the beam is coming from and is independent of the wavelength, which makes the states of the outgoing beams corresponding to λ_1 and λ_2 different. The interferograms are modulated in the direction orthogonal to the dispersion plane. In the simulations in this paper, when $\lambda_1 > \lambda_0$, the interferogram is deflected clockwise and the impact spectrum of the 2D power spectrum is located in the first and third quadrants; when $\lambda_2 < \lambda_0$, the interferogram is deflected counterclockwise and the impact spectrum is located in the second and fourth quadrants.

3. Simulation Experiments and Results

The system was simulated using ZEMAX. We used a structure that has a simplified motion control system, as shown in Figure 5. The parameters of some components are given in Section 2.3 and the dimensions of the optics of the interferometer are shown in Table 1. A 40 mm × 10 mm rectangular light source with collimation characteristics is selected, eliminating the setting of entrance optics. The imaging lenses are designed as

object-space telecentric lenses. The aperture stop is set at the focal plane of the imaging system to act as a band-pass filter.

Table 1. The geometrical dimensions of the optics of the interferometer in the simulation.

Components	Dimensions
Cube beam splitter (50:50)	60 mm × 60 mm × 60 mm
Mirror 1	50 mm × 60 mm
Bimirror *	35 mm × 60 mm
Right-angle prism *	70 mm × 70 mm
Prisms 1 and 2	50 mm × 25 mm × 28.87 mm
Bimirror assembly *	40 mm × 40 mm
Mirror 2	44 mm × 74 mm

* These optics are sized for each reflecting surface.

First, the wavelength of the incident light is set to 390 nm and the Littrow wavelength is set to 398 nm (the angle of mirror 2 tilt is set to 20.99° according to Section 2.4 and the bimirror assembly is tilted at twice the angle of mirror 2). The interferogram received by the detector, the 2D power spectrum obtained by 2D Fourier transform of the 2D interferogram, and the 1D spectrum obtained by 1D Fourier transform of the 1D interferogram are shown in Figure 6; the upper half of the interferogram is the 2D interferogram and the lower half is the 1D interferogram. Since the impact spectrum of the 2D power spectrum is located in the second and fourth quadrants, only the portion of the 1D spectrum that is smaller than the Littrow wavelength is intercepted. From the 1D spectrum, the full width at half maximum (FWHM) is about 0.019 nm, which is close to the theoretical maximum spectral resolution of 0.014 nm calculated from Equation (12).

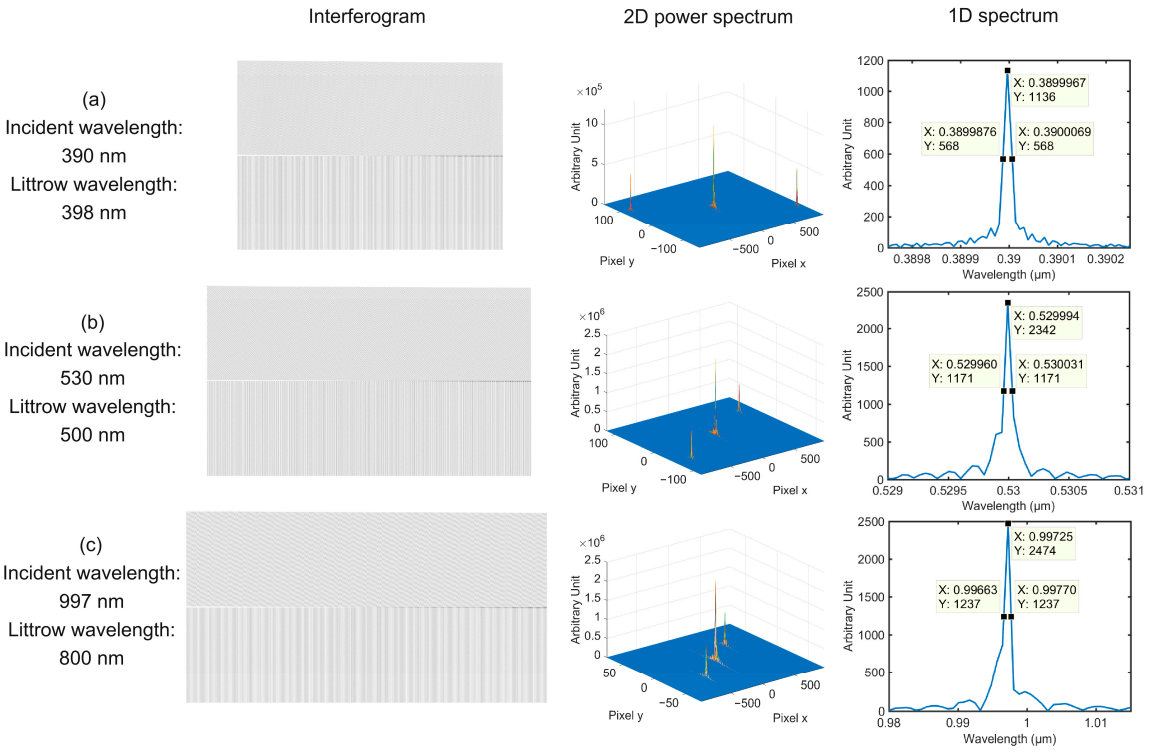

Figure 6. Results of simulation at different wavelengths.

Similarly, set the incident light wavelengths to 530 nm and 997 nm and repeat the work above. The FWHM values are about 0.071 nm and 1.07 nm, respectively, while

the corresponding theoretical maximum spectral resolutions are 0.061 nm and 0.72 nm, respectively. The spectral resolving power obtained from the simulation is smaller than the theoretical spectral resolving power, which is a normal phenomenon. This discrepancy is mainly due to asynchronous sampling.

To verify the constancy of the FLP location, we can observe the patterns on the detector. If the FLP is not optically conjugated to the detector plane, the beams from the two arms do not completely overlap at the detector plane and there should be regions around the interferogram where the irradiance is not zero that have no fringes. Therefore, the interferograms in Figure 6 verify that the FLPs of different wavelengths are all precisely located at the optical conjugate plane of the detector plane.

To verify the FOV, a 1D interferogram of the limiting off-axis rays is traced in ZEMAX. The wavelength is set to 397 nm because the usable FOV at this wavelength is close to that of the instrument and the interference curve is easy to observe. The angles of the off-axis rays are calculated according to Equation (14); for example, $\phi = 0.052^\circ$ and $\varphi = 0.1^\circ$. Figure 7a shows the interference curves for the on-axis rays and the limiting off-axis rays. The 0th pixel is the center of the detector. It shows that the OPD changes by about 1/2 of the wavelength at the edge of the fringe pattern, which is consistent with the theoretical result. To verify that the usable FOV of the instrument is applicable across the spectral range, another wavelength of 825 nm is set, as shown in Figure 7b. The OPD changes less than 1/2 of the wavelength. To verify that the usable FOV also applies to 2D interferograms, the curves of a row of the 2D interferograms at 397 nm are shown in Figure 7c. The OPD changes by about 1/2 of the wavelength.

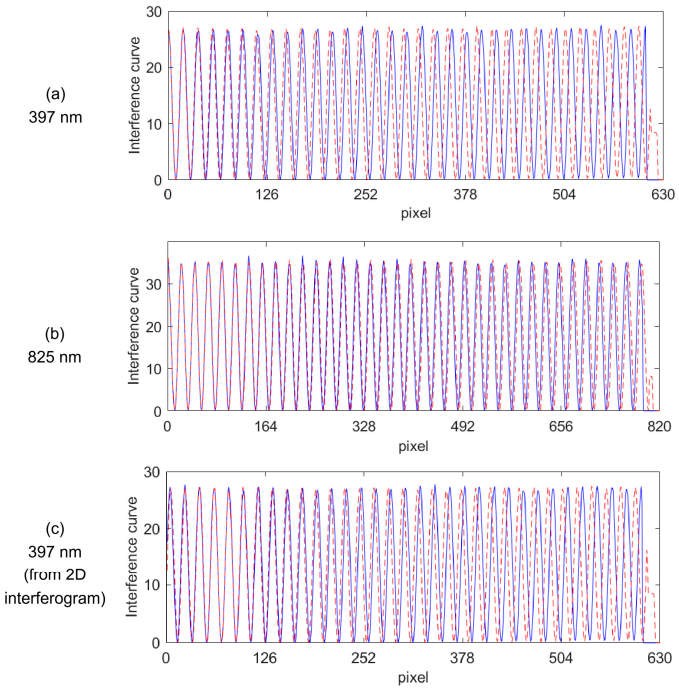

Figure 7. Interference curve of the on-axis rays (solid line) and the limiting off-axis rays (dashed line).

4. Conclusions

In this paper, we address the problem in current designs of prism-based SHSs: the FLP moves with changes in wavelength. We propose a design of a prism-based TSHS that maintains a constant FLP location and has a dual output system, utilizing a prism–bimirror–mirror structure. The theoretical spectral resolving power is higher than 1300 in the spectral range from 10,000 cm^{-1} to 25,641 cm^{-1} and higher than 10,000 in the spectral range from 20,000 cm^{-1} to 25,641 cm^{-1}, based on an example. Additionally, we design an

orthogonal TSHS in the form of a Mach–Zehnder interferometer to simplify the motion control system. Given its ability to retain the advantages of prism-based SHSs as well as to eliminate the need to calculate the FLP location and move the imaging device based on the predicted wavelength of incident light during use, this optical implementation shows good potential for the further development and practical application of SHS, particularly when a broadband spectrum is required. Moreover, methods to improve the FOV and spectral resolving power of prism-based SHSs need further research.

Author Contributions: Conceptualization, Z.L. and D.Z.; methodology, Z.L. and D.Z.; software, Z.L.; validation, Z.L. and C.H.; formal analysis, Z.L., H.Y. and D.Z.; investigation, Z.L. and D.Z.; resources, H.Y. and C.H.; data curation, C.H. and H.Y.; writing—original draft preparation, Z.L.; writing—review and editing, Z.L. and D.Z.; visualization, H.Y. and Z.L.; supervision, C.H.; project administration, D.Z.; funding acquisition, D.Z. All authors have read and agreed to the published version of the manuscript.

Funding: This research was funded by National Natural Science Foundation of China (NSFC) project (No.41405021) and China Manned Space Engineering Project (No.GE1215).

Institutional Review Board Statement: Not applicable.

Informed Consent Statement: Not applicable.

Data Availability Statement: The raw data supporting the conclusions of this article will be made available by the authors on request.

Conflicts of Interest: The authors declare no conflicts of interest.

References

1. Dohi, T.; Suzuki, T. Attainment of high resolution holographic fourier transform spectroscopy. *Appl. Opt.* **1971**, *10*, 1137–1140. [CrossRef] [PubMed]
2. Zhang, W.L.; Liu, Z.Y.; Wang, H.; Chen, Y.; Wang, Y.; Zhao, Z.Z.; Sun, T. Research status of spatial Heterodyne spectroscopy-A review. *Microchem. J.* **2021**, *166*, 106228. [CrossRef]
3. Harlander, J.M.; Lawler, J.E.; Corliss, J.; Roesler, F.L.; Harris, W.M. First results from an all-reflection spatial heterodyne spectrometer with broad spectral coverage. *Opt. Express* **2010**, *18*, 6205–6210. [CrossRef] [PubMed]
4. Lenzner, M.; Diels, J.-C. A Sagnac Fourier spectrometer. *Opt. Express* **2017**, *25*, A447–A453. [CrossRef] [PubMed]
5. Nirmal, K.; Rengaswamy, S.; Sriram, S.; Murthy, J.; Ambily, S.; Safonova, M.; Sreejith, A.G.; Mathew, J.; Sarpotdar, M. Design and modeling of a tunable spatial heterodyne spectrometer for emission line studies. *J. Astron. Telesc. Instrum. Syst.* **2018**, *4*, 25001. [CrossRef]
6. Chu, Q.H.; Li, X.T.; Jirigalantu; Sun, C.; Chen, J.; Wang, J.N.; Sun, Y.Q.; Bayanheshig. Design study of a cross-dispersed spatial heterodyne spectrometer. *Opt. Express* **2022**, *30*, 18854–18855, Erratum in *Opt. Express* **2022**, *30*, 10547. [CrossRef] [PubMed]
7. Németh, G.; Pekker, A. New design and calibration method for a tunable single-grating spatial heterodyne spectrometer. *Opt. Express* **2020**, *28*, 22720–22731. [CrossRef] [PubMed]
8. Cai, Q.S.; Bin, X.L.; Huang, M.; Han, W.; Pei, L.L.; Bu, M.X. Prototype development and field measurements of high etendue spatial heterodyne imaging spectrometer. *Opt. Commun.* **2018**, *410*, 403–409. [CrossRef]
9. Sahoo, A.; Mathew, J.; Battisti, A.; Tucker, B. Compact Spatial Heterodyne Spectrographs for Future Space-Based Observations: Instrument Modeling and Applications. *Sensors* **2024**, *24*, 4709. [CrossRef] [PubMed]
10. Wang, Q.; Luo, H.; Li, Z.; Ding, Y.; Xiong, W. High dynamic range spatial heterodyne one-dimensional imaging spectroscopy based on a digital micromirror device. *Opt. Express* **2024**, *32*, 22067–22077. [CrossRef] [PubMed]
11. Sun, Y.Q.; Li, X.T.; Galantu, J.; Chu, Q.H.; Chen, J.; Li, F.G.; Song, N.; Wang, G.; Ni, Q.L. Development of a Spatial Heterodyne Terahertz Raman Spectrometer with Echelle Gratings. *Appl. Sci.* **2023**, *13*, 967. [CrossRef]
12. McCormack, E.A.; Hugh Mortimer, A.; Ciaffoni, L. Compact spatially heterodyned static interferometer. *Appl. Opt.* **2020**, *59*, 4271–4278. [CrossRef] [PubMed]
13. Maione, B.D.; Luo, D.; Miskiewicz, M.; Escuti, M.; Kudenov, M.W. Spatially heterodyned snapshot imaging spectrometer. *Appl. Opt.* **2016**, *55*, 8667–8675. [CrossRef] [PubMed]
14. Chu, Q.H.; Li, X.T.; Jirigalantu; Chen, J.; Sun, Y.Q. Design and theoretical analysis of a conical-diffraction-based cross-dispersed spatial heterodyne spectrometer. *Results Phys.* **2023**, *48*, 106427. [CrossRef]

15. Fessler, K.A.S.; Waldron, A.; Colón, A.; Carter, J.C.; Angel, S.M. A demonstration of spatial heterodyne spectrometers for remote LIBS, Raman spectroscopy, and 1D imaging. *Spectrochim. Acta Part B-At. Spectrosc.* **2021**, *179*, 106108. [CrossRef]
16. Frassetto, F.; Cocola, L.; Zuppella, P.; Deppo, V.D.; Poletto, L. High sensitivity static Fourier transform spectrometer. *Opt. Express* **2021**, *29*, 15906–15917. [CrossRef] [PubMed]
17. Lenzner, M.; Diels, J.-C. Concerning the Spatial Heterodyne Spectrometer. *Opt. Express* **2016**, *24*, 1829–1839. [CrossRef] [PubMed]
18. Frassetto, F.; Cocola, L.; Zuppella, P.; Da Deppo, V.; Poletto, L. Static, refractive and monolithic Fourier transform spectrometer: Development and prototyping. *Sci. Rep.* **2024**, *14*, 1164. [CrossRef] [PubMed]
19. Ye, S.; Shi, X.Z.; Li, S.; Wang, J.J.; Wang, X.Q. Study on Prism-Based Spatial Heterodyne Spectrometry. *Acta Opt. Sin.* **2019**, *39*, 1130002. [CrossRef]
20. Li, Y.X.; Huang, Y.; Wu, Y.H.; Li, H.C.; Yang, X.H.; Li, Z.F.; Zhang, Z.H. Design of orthogonal tunable spatial heterodyne spectrometer based on prism dispersion. *Opt. Lasers Eng.* **2023**, *162*, 107390. [CrossRef]